

MAC: Magnetostatic Active Contour Model

Xianghua Xie, *Member, IEEE* and Majid Mirmehdi, *Member, IEEE*

Abstract—We propose an active contour model using an external force field that is based on magnetostatics and hypothesized magnetic interactions between the active contour and object boundaries. The major contribution of the method is that the interaction of its forces can greatly improve the active contour in capturing complex geometries and dealing with difficult initializations, weak edges and broken boundaries. The proposed method is shown to achieve significant improvements when compared against six well-known and state-of-the-art shape recovery methods, including the geodesic snake, the generalized version of GVF snake, the combined geodesic and GVF snake, and the charged particle model.

Index Terms—Active contours, deformable model, object segmentation, magnetostatic forces

1 INTRODUCTION

ACTIVE contour or snake based methods have been widely used for shape recovery due to their natural handling of shape variation, e.g. [1]–[3]. Their design normally involves the consideration of the following three fundamental issues: contour representation and its numerical solution, object boundary description and stopping function design, and initialization and convergence.

1.1 Contour representation and numerical method

Contour representation involves the decision whether to use a parametric or implicit representation. Parametric active contours are usually represented as polynomials or splines, e.g. [4], [5], and interpolated using landmarks. They suffer from topological issues as it is difficult to determine the evolution of the contour crossing points and its reparameterization after every topological change, hence, predefined topology adaptations are usually necessary, e.g. [6]. The selection of landmarks is also non-trivial and critically influences shape description. Implicit representations, on the other hand, do not explicitly interpolate the contours. Instead, they embed the contour into another function, which is then temporally adapted to affect snake deformations. The Level Set method [7] is the most widely used technique to implicitly represent active contours that handle topological changes. The snake is embedded in the zero level set and its temporal evolution is achieved by deforming the entire level set function. It can naturally model contour propagation and topological changes, however, it is generally slower than parametric methods as the deformation of a higher dimensional function is necessary. Very recently Morse *et al.* [8] proposed to implicitly represent active contours using radial basis

functions (RBFs) by placing RBFs at snake landmarks. This then avoids manipulating a higher dimensional function, however, it requires dynamic insertion and deletion of landmarks. Similar to parametric representation, the resolution of the landmarks can affect the accuracy of contour representation.

While choosing a representation scheme, one also needs to select appropriate numerical methods to solve the contour evolution equation. The Finite Element Method [9] is the common technique used in parametric snake models, while the Finite Difference Method [7] is mostly used in implicit snake models to numerically solve the partial differential equations (PDEs). Alternative approaches do exist, amongst them [10] which adopted the stochastic dynamics of interface propagation into the level set framework.

1.2 Object boundary description and stopping function design

These functions determine where the contours are expected to be attracted to and be stabilized at. Boundary description using the image gradient is the most commonly used technique e.g. [1], [2], [11]–[13], which assumes object separation by way of intensity discontinuities. This often results in broken edges and weak boundaries due to the lack of global information. Techniques such as anisotropic smoothing [14] can be used to enhance and refine the boundaries.

On the other hand, region-based techniques such as [3], [15]–[18], generally use more global information to define object boundaries. Zhu and Yuille [15] proposed a region competition approach by performing statistical tests while growing multiple regions independently and using a minimum description length (MDL) criteria to minimize the overlapping of the growing regions competing for neighboring pixels. In [3], Paragios and Deriche used a bank of isotropic Gaussian filters, LoG filters, and Gabor filters to extract textural features modeled using a mixture of Gaussians. Their region-based snake segmentation then was based on the maximization of *a posteriori* probabilities. Wang and Vemuri [19]

X. Xie is with the Department of Computer Science, University of Wales Swansea, Faraday Tower, Singleton Park, Swansea SA2 8PP, UK. E-mail: xie@cs.bris.ac.uk.

M. Mirmehdi is with the Department of Computer Science, University of Bristol, MVB, Woodland Road, Bristol BS8 1UB, UK. E-mail: majid@cs.bris.ac.uk.

proposed an active contour model based on tensor field segmentation using a piecewise constant region model. These techniques are generally application dependent, need some prior knowledge of the objects of interests, and like other region segmentation methods are liable to over-segment or under-segment the object.

There have also been attempts to bridge boundary and region-based techniques, e.g. [19]–[22]. For example, Chakraborty *et al.* [21] integrated region segmentation and gradient based boundary information in a Bayesian framework, while Xie and Mirmehdi [22] used diffused region forces to prevent the snake from leaking through weak edges. One of the main challenges for integrated approaches is that the region and boundary information may not locally correspond.

1.3 Initialisation and convergence

As snakes generally provide locally minimized solutions, it is a great challenge to achieve initialization invariancy and robust convergence, particularly for boundary based methods. The problem is compounded when the snake has to deal with complex topologies and concave shapes.

Methods that rely directly on the boundary gradient inevitably have very limited capture range and are not able to reach deeper concavities. Using the distance transform to obtain a distance vector flow (DVF) was one attempt to enlarge the capture range [9], but this still has difficulties with concave shapes. Caselles *et al.* [1] introduced the constant flow into the geometric active contour model to speed up its convergence and to pull or push the active contour towards object boundaries. However, this only monotonically expands or shrinks the contour. The weighted area functional addition to the geodesic snake by Siddiqi *et al.* [11] also did not provide a satisfactory solution to convergence on weak edges [23]. Xu and Prince [2], [24] iteratively diffused the edge gradient vector to significantly enlarge the capture range and increase the ability to reach concavities. Their snake was initialized across the object boundary due to the bidirectional nature of the vector field, where vectors point towards the object boundary from both sides. This can prevent the snake from leaking through small boundary holes or weak edges, but only to some degree. Also, bidirectionality can cause their contours to collapse on approach to the same object boundary. More importantly, Xu and Prince's GVF/GGVF active contours fail to evolve at saddle points, i.e. when the contour is tangent to the force vector. This can be demonstrated using the four-disc problem in Fig. 1 where there are four saddle points (indicated in dark red) and five stationary points (in light green) in the GGVF vector map (final results in Fig. 4). These critical points are commonly found in real images when using GVF/GGVF force fields, greatly restraining their application to real world problems.

There have been several attempts to solve the convergence issue. Paragios *et al.* [12] added the constant

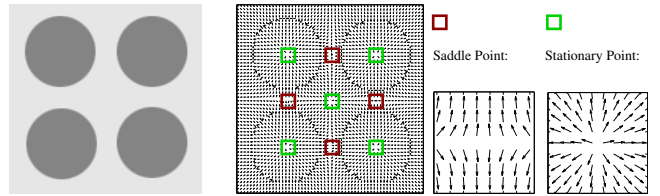


Fig. 1. The four-disc problem - from left: An image contains four discs, the GGVF vector map, enlarged saddle point (red square) and stationary point (green square).

flow to the GVF model which pushes the active contour when it is close to tangent to the underlying vector. This however can not deal with stationary points, e.g. the center of the image in the four-disc problem in Fig. 1. Li *et al.* [13] suggested the active contour be split along stationary and saddle points but this strategy is inappropriate when the active contour is initialized inside or crosses the object boundary. Gil and Radeva [25] proposed the curvature vector flow (CVF), derived from a curvature dependent distance transform, to push the contour into concavities. Their method only reduces the number of stationary or saddle points and can not completely eliminate them. Moreover, *it requires there be no gaps in the object boundary*. Very recently, Li and Acton [26] proposed convolving the image edge map with a vector field kernel, which comprises radial symmetric vectors pointing towards the center of the kernel. This is equivalent to assigning an attraction force for each pixel position, based on which the snake is evolved. The authors have shown better initialization and noise insensitivity. However, it is still a stationary vector field which will suffer from the convergence issues discussed above.

Combined optimization techniques have also been used to improve initialization invariancy and convergence ability. Boykov and Kolmogorov [27] considered the segmentation problem as finding geodesics, similar to [1], but using graph cuts to find the global minimum. This exhibits less sensitivity to initialization, but graph cuts tend to choose shorter cuts which may result in inaccurate segmentation. Similar ideas have been explored by others, e.g. see [28].

Recently, Jalba *et al.* [29] proposed a charged particle model (CPM) based on electrostatics. The particles are attracted towards object boundaries due to the potential forces while being repelled by each other. The authors demonstrated that the particles could be initialized randomly across the image and did not suffer from convergence issues related to GVF/GGVF as particles once attracted to the boundaries would move along the boundary under the influence of the repulsive force. However, as shown in [30], particles on weak edges will be attracted to nearby strong edges resulting in broken contours. The method also frequently involves particle insertion and deletion, and is computationally expensive. Yang *et al.* [30] migrated this particle model to a con-

tour model by using similar, but conditionally imposed, attraction and repellent forces. Their model showed improvements on the original CPM, the geodesic, and the GVF snakes.

-*-

The three issues discussed above are not always independent of each other. An appropriate snake representation ensures the snake handles the deformations properly, however, representation schemes that support topological changes do not necessarily always achieve the desired contour evolutions. Better boundary description can improve convergence ability by preventing the contour from leaking through and good convergence ability is paramount to not compromise any gains from carefully chosen contour representation and boundary extraction. On the other hand, good convergence properties can compensate certain inadequacies in boundary description, e.g. bidirectional forces can stabilize contours at weak edges. In this paper, we show that using a novel contour evolution force can achieve significant improvement in initialization invariancy and convergence ability, even when using very simple boundary descriptions directly based on the image gradient.

In [31], we proposed a snake external force field based on magnetostatics. We hypothesized magnetic interactions between the active contours and the object boundaries, resulting in a magnetic field that can push the contours to object boundaries. A simplified snake model was only applied to *synthetic* boundaries to illustrate the convergence ability of the model. In this paper, we present the full Magnetostatic based Active Contour (MAC), including force field generation, edge preserving magnetic field diffusion, and its fast implementation. Furthermore, we present a comparative analysis of MAC against several state-of-the-art deformable models.

We note recent independent work by Xiang *et al.* [32] proposed a physically motivated active contour model inspired by the elastic interaction between line defects in solids. They used different degrees of image smoothing by varying the Gaussian convolution kernel and running independent snake segmentation for each smoothed image. Final segmentation was obtained by comparing these independent segmentations followed by contour shortening based on curvature flow. Xiang *et al.*'s simplified long range force between the object boundaries and the active contour takes a similar form to our magnetic force in [31]. However, the MAC model is more intuitive, and uses different strategies to perform initialization and to handle image noise.

The main contributions of this work can be summarized as follows:

- 1) A novel external force using global pixel interactions is introduced as a *boundary* based snake model. This force field is generated based on hypothesized electro-magnetic interactions between image edge pixels. Unlike traditional boundary based snakes which examine edge strength locally

to decide whether to keep evolving or to converge, the MAC model utilizes edge pixel interactions across the whole image which provides a more global view of object boundary representation.

- 2) Significant improvements have been achieved with the proposed force field upon *boundary* based snake models. Comparative experimental results have demonstrated superior performance in initialization invariancy and convergence ability, as well as recovering broken boundaries and weak edges, compared to several traditional and state-of-the-art *boundary* based snake methods. This has been our main objective.
- 3) The proposed *boundary* based snake method has also shown comparable performance to much more sophisticated *region* based approaches. The proposed MAC model exhibits similar initialization and convergence properties to region based techniques, but imposes simpler assumptions and requires less prior knowledge. MAC snake can also recover shapes with broken boundaries or even disconnected parts, which is generally difficult for region based methods. However, the MAC model is not intended to compete against or replace region based methods, but provides a good alternative to those methods for object segmentation, particularly when prior knowledge is incomprehensive or difficult to obtain.
- 4) An edge preserving method is proposed to enhance the snake performance in the face of noise interference.
- 5) Fast, yet accurate, computational methods are presented for efficient implementation of the MAC model, which is potentially beneficial for a variety of methods and applications.

Section 2 gives a brief introduction to the six external force fields we compare against. The proposed method is then described in Section 3. Experimental results and comparative studies appear in Section 4. Section 5 concludes the paper.

2 BACKGROUND

Here we briefly review six boundary based deformable models which we shall later apply to for comparison against our proposed method. All the models come with certain advantages and disadvantages. In what follows, f is the gradient magnitude of image I , \mathbf{x} is a pixel position, $\hat{\mathbf{N}}$ is the unit inward normal of the evolving contour, and κ denotes the curvature.

2.1 Distance vector flow (DVF) snake

The Euclidean distance transform $\mathcal{D}(\mathbf{x})$ is computed to find the nearest distance to the object boundary for each pixel position \mathbf{x} . In [9], Cohen and Cohen used the Chamfer distance, which approximates the Euclidean distance, to derive this external force for the active

contour. The DVF field is given as $-\nabla\mathcal{D}(\mathbf{x})$ and the active contour is then stated as:

$$C_t = \alpha g(\mathbf{x})\kappa\hat{\mathbf{N}} - (1 - \alpha)(\nabla\mathcal{D}(\mathbf{x}) \cdot \hat{\mathbf{N}})\hat{\mathbf{N}}, \quad (1)$$

where α is a real constant, and $g(\mathbf{x}) = 1/(1 + f(\mathbf{x}))$, commonly known as the stopping function.

2.2 Geodesic snake

The image dependent constant flow can be formulated as $C_t = g(\mathbf{x})\hat{\mathbf{N}}$. This shows each point on the contour moving in the direction of its normal at a speed proportional to $g(\mathbf{x})$. It monotonically shrinks or expands the contour towards the object boundary and plays an important role in both the geodesic snake model introduced by Caselles *et al.* [1], and in later incremental improvements, such as [11]. The geodesic snake is formally given as:

$$C_t = g(\mathbf{x})(\alpha\kappa + c)\hat{\mathbf{N}} - (\nabla g(\mathbf{x}) \cdot \hat{\mathbf{N}})\hat{\mathbf{N}}, \quad (2)$$

where c is a constant controlling the contribution of the constant flow. The second term of (2) acts like a doublet, which attracts the snake closer to the object boundary.

2.3 Generalised gradient vector flow (GGVF) snake

The parametric GVF [24] and its generalized version GGVF [2] introduced by Xu and Prince have been widely used in active contour models as external forces, e.g. [33]. The GGVF field, $\tilde{\mathbf{v}}(\mathbf{x})$, is defined as the equilibrium solution of the partial derivatives of:

$$\mathbf{v}_t(\mathbf{x}) = p(|\nabla f(\mathbf{x})|)\Delta\mathbf{v}(\mathbf{x}) - q(|\nabla f(\mathbf{x})|)(\mathbf{v} - \nabla f(\mathbf{x})), \quad (3)$$

where the initial vector field $\mathbf{v}(\mathbf{x}, t = 0) = \nabla f(\mathbf{x})$, and $p(\cdot)$ and $q(\cdot)$ are monotonically non-increasing and non-decreasing functions respectively, controlling the amount of diffusion. These two functions are selected such that $p(\cdot)$ gets smaller as $q(\cdot)$ becomes larger with the desired result that in the proximity of large gradients, there will be very little smoothing and the vector field will be nearly equal to $\nabla f(\mathbf{x})$, i.e. $p(|\nabla f(\mathbf{x})|) = e^{-\frac{|\nabla f(\mathbf{x})|}{K}}$ and

$q(|\nabla f(\mathbf{x})|) = 1 - p(|\nabla f(\mathbf{x})|)$, where K is a constant and acts as a trade-off between field smoothness and gradient conformity. The GGVF active contour can then be defined as:

$$C_t = \alpha g(\mathbf{x})\kappa\hat{\mathbf{N}} + (1 - \alpha)(\tilde{\mathbf{v}}(\mathbf{x}) \cdot \hat{\mathbf{N}})\hat{\mathbf{N}}. \quad (4)$$

2.4 Geodesic GVF/GGVF (GeoGVF/GeoGGVF) snake

In [12], Paragios *et al.* integrated the GVF with the geodesic active contour model, referred to here as GeoGVF. The GVF provides the bidirectional force to drive the contours towards edges, while the constant flow from the geodesic model poses conditional inflation or deflation forces on the contour. The two forces are mutually exclusive [12]:

$$C_t = g(\mathbf{x}) \left(\alpha\kappa + (1 - |H(\mathbf{x})|)\tilde{\mathbf{v}}(\mathbf{x}) \cdot \hat{\mathbf{N}} + H(\mathbf{x}) \right) \hat{\mathbf{N}}, \quad (5)$$

where the weighting function $H(\mathbf{x})$ is $H(\mathbf{x}) = sign(\tilde{\mathbf{v}}(\mathbf{x}) \cdot \hat{\mathbf{N}})e^{-\delta|\tilde{\mathbf{v}}(\mathbf{x}) \cdot \hat{\mathbf{N}}|}$, and δ is a scaling factor. The additional adaptive bidirectional constant force is designed to determine the curve propagation when the GVF term becomes inactive, e.g. at saddle points. GGVF generally outperforms GVF [2], and as such we implement this method with GGVF instead of GVF. We shall refer to it as GeoGGVF.

2.5 Curvature vector flow (CVF) snake

Gil and Radeva [25] proposed a new distance transform using a modified mean curvature flow. The curvature vector flow was then computed from this distance transform to attract contours into shape concavities¹. Their principal idea was to evolve the object boundaries according to curvature flow till they were no longer concave. The inward or outward propagation was defined by monotonically non-negative or non-positive curvature flow such that, $f_t = \max(\kappa, 0)\hat{\mathbf{N}}$ on inward propagation, and $f_t = \min(\kappa, 0)\hat{\mathbf{N}}$ on outward propagation. A distance map $\mathcal{D}^\kappa(\mathbf{x})$ was then obtained by tracing back the evolution of the boundary from which the curvature vector flow, $-\nabla\mathcal{D}^\kappa(\mathbf{x})$, was derived. The CVF active contour is then:

$$C_t = \alpha g(\mathbf{x})\kappa\hat{\mathbf{N}} - (1 - \alpha)(\nabla\mathcal{D}^\kappa(\mathbf{x}) \cdot \hat{\mathbf{N}})\hat{\mathbf{N}}. \quad (6)$$

It is worth noting that for the CVF snake, the object boundary has to be closed, otherwise, pre-processing is required to close any gaps.

2.6 Charged particle model (CPM)

CPM is based on the theory of charged particle dynamics, consisting of a set of positively charged particles moving in the image domain and interacting with negative fixed charges proportional to image gradients. These positive particles are attracted towards the fixed charges under the influence of a mesh-to-particle (Lorentz) force, $\mathbf{F}_L(c_x) = \frac{q}{4\pi\epsilon} \sum_{y \in \Omega, y \neq x} e_y \frac{\hat{\mathbf{R}}_{xy}}{R_{xy}^2}$ and repelled by each other by the repulsive particle-to-particle (Coulomb) force, $\mathbf{F}_C(c_x) = \frac{q^2}{4\pi\epsilon} \sum_{x' \in \Omega, x' \neq x} \frac{\hat{\mathbf{R}}_{xx'}}{R_{xx'}^2}$ where q is a positive charge assigned to free particle c at position x moving in a 2D discrete domain Ω , e_y is a fixed negative charge assigned at position y , ϵ is the permittivity constant, and $\hat{\mathbf{R}}_{xy}$ denotes the unit distance vector between x and y with distance R_{xy} . The integrated force, \mathbf{F}_i , acting on the particle c_x is:

$$\mathbf{F}_i(c_x) = w_1 \mathbf{F}_L(c_x) + w_2 \mathbf{F}_C(c_x) + \beta \mathbf{F}_d(c_x), \quad (7)$$

where $\mathbf{F}_d(c_x) = -\mathbf{v}_{cx}$ is the damping force required to attain a stable equilibrium state, \mathbf{v}_{cx} is the particle speed, and w_1, w_2, β are weighting parameters for the attraction, the repulsion, and the damping forces, respectively. These three parameters need to be tuned such that

1. Note that the curvature vector flow is different from the well-known curvature flow.

$w_2 > w_1 > \beta$. CPM uses a multiscale process to ensure the particles spread across the image. The particles are then gradually attracted to boundaries according to (7) and advance along the boundaries, with proper particle addition and deletion during their movement. Once the particles have stabilized, “curve” reconstruction is necessary in order to obtain the object boundary representation.

MAC, described next, shows significant improvements on all the above techniques.

3 PROPOSED METHOD

As demonstrated in [2], [13], [23]–[25], bidirectionality is a very useful feature for an external force field as it facilitates more arbitrary, cross boundary initialization and improves the snake’s performance towards weak edges and broken boundaries. However, the vector force fields in all these works are stationary. This means almost inevitably, there exist critical points, such as saddle points, that prevent the snake from continued propagation towards object boundaries.

Combining multiple force fields each with its different influences on a contour’s evolution is a common way to improve snake evolution, e.g. [12], [30]. In both of these works, an external force field is pre-computed as the basis for manipulating snakes, i.e. the GVF in [12] and the attraction force field in [30]. These force fields are stationary and independent of the snake evolution. Later, as their snake deforms, these force fields are modified according to the snake’s position. In the case of [12] a weighted balloon force, borrowed from the geodesic snake, is used to influence the contour deformation. However, the direction of the balloon force at each contour position is merely a projection of the GVF vector on to the snake normal. As shown later in Section 4, this combination can not sufficiently resolve the problems related to the vector field itself. In [30], an image dependent competition force exerted by the snake itself as it moves is combined with the stationary attraction force to obtain a dynamic force field. However, the balance between the attraction force and the competition force in this technique is critical for successful convergence and sometimes requires careful tuning.

Our approach is to define a novel, *single*, external bidirectional force field which has the ability to dynamically update itself while the contour evolves. This is significantly different from other works and we reemphasize that it does not involve the introduction of any extra forces to mobilize the force field. In brief, we hypothesize electric currents flowing through both the object boundary and the active contour. The magnetic fields generated by each of the currents will interact and cause a force between them. This magnetic vector field behaves as an external force to push or pull the contour towards the object boundary. Although the magnetic field caused by the image gradient is stationary, the force it imposes on the snake is dependent on the snake’s evolution. Thus

the force field is dynamically changing along with the snake. We show that by using this electromagnetic interaction analogy the snake is then much less sensitive to its initial position and much more robust towards complex geometries and topologies. Next, we present the basic theory of magnetostatics which is used to provide the analogy for MAC. The Level Set method is then used to implicitly represent and evolve MAC.

3.1 The magnetostatic field

Consider two points P and Q with charges, q_P and q_Q , and velocity vectors \mathbf{u}_P and \mathbf{u}_Q respectively. The magnetostatic force exerted upon q_P due to q_Q is [34]:

$$\mathbf{F}_{QP} = q_P \mathbf{u}_P \times \mathbf{B}_P, \quad \mathbf{B}_P = \mu_0 q_Q \mathbf{u}_Q \times \frac{\hat{\mathbf{R}}_{QP}}{4\pi R_{QP}^2}, \quad (8)$$

where \mathbf{B}_P is known as the magnetic flux density at point P due to the point charge at Q , μ_0 is the permeability constant, R_{QP} is the distance between the two charges, $\hat{\mathbf{R}}_{QP}$ is their unit distance vector, and \times denotes the cross product. The magnetic field \mathbf{H} is then defined as $\mathbf{H} = \mu_0^{-1} \mathbf{B}_P$. It is clear that $q\mathbf{u}$ can be viewed as an elementary current introduced by a moving charge. In order to obtain the magnetic field introduced by a current, we consider infinitesimal current segments $d\mathbf{l}_P$ and $d\mathbf{l}_Q$ at P and Q on loops C_1 and C_2 with electric currents I_1 and I_2 respectively (see Fig. 2). The total force on $d\mathbf{l}_P$ due to current I_2 is then:

$$d\mathbf{F}_P = I_2 d\mathbf{l}_P \times \mathbf{B}_P, \quad (9)$$

where \mathbf{B}_P is re-written as:

$$\mathbf{B}_P \equiv \frac{\mu_0}{4\pi} I_2 \oint_{C_2} d\mathbf{l}_Q \times \frac{\hat{\mathbf{R}}_{QP}}{R_{QP}^2}, \quad (10)$$

commonly known as the Biôt-Savart Law. It defines how the magnetic flux density is obtained from a given current. In Fig. 2, the red ‘+’ symbols denote the magnetic field going perpendicularly into the image plane and the blue ‘.’ symbols denote the magnetic field coming out of the image plane. These symbols represent the overall magnetic field due to current I_2 . The magnetic force $d\mathbf{F}_P$ at position P on C_1 is in its outward normal direction. Next, we make an analogy of these principles in our active contour model.

3.2 The MAC model

Magnetostatic theory is applied to our active contour model by charging both the object boundary and the active contour with electric currents. The concept is represented again in Fig. 2 by treating C_1 as an active contour and C_2 as an object boundary. As we are interested in the deformation of the contours, only the forces exerted by the object boundary on the active contour are needed. In other words, we shall ignore magnetic forces introduced by the active contour. We then obtain an estimation of the hypothesized direction

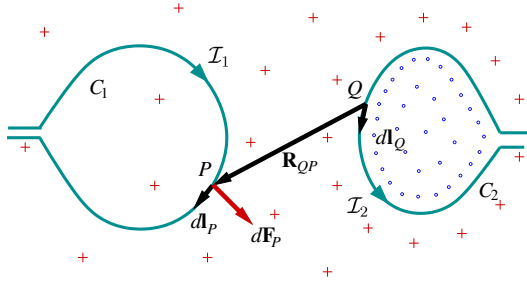


Fig. 2. Magnetic force between two currents - see text for details.

of the currents in the object boundary and the active contour, and compute the resulting magnetic flux density at each pixel position in the image using (10). Based on this field the active contour drives towards the object boundary according to (9).

The direction of current for the object boundary can be computed using boundary orientation estimation. Let $I_x(\mathbf{x})$ and $I_y(\mathbf{y})$ be the partial derivatives in x and y for image I . This gradient vector field, $(I_x(\mathbf{x}), I_y(\mathbf{y}))$, contains vectors that are locally perpendicular to edges. Thus, the boundary orientation, $\mathbf{O}(\mathbf{x})$, can be conveniently obtained by a 90° rotation of the normalized gradient vectors $(\hat{I}_x(\mathbf{x}), \hat{I}_y(\mathbf{x}))$:

$$\mathbf{O}(\mathbf{x}) = (-1)^\lambda (-\hat{I}_y(\mathbf{x}), \hat{I}_x(\mathbf{x})), \quad (11)$$

where $\lambda = 1$ gives an anti-clockwise rotation in the image coordinates, and $\lambda = 2$ provides a clockwise rotation. This is then assigned as orientation of current in the object boundary.

In a similar fashion, the direction of current for the active contour is given based on the estimation of the contour orientation. However, as we are using a level set representation, the contour is already embedded in a 3D surface Φ , obtained from the signed distance transform on the contour. No extra preparation is therefore necessary other than similarly rotating the gradient vector $\nabla\Phi$ of the level set function either in a clockwise or anti-clockwise direction. As a result, these rotated vectors with hypothesized electric currents will interact with each other according to (9) and (10) as illustrated in Fig. 2. The rotated gradient vectors given in (11) attract nearby contour segments that have the same current direction and repulse those that have the opposite. This means a value of 1 or 2 for λ results in opposing contour propagation. We discuss this later in Section 4 where we also show how to use both λ values simultaneously.

Next, we can work out the magnetic flux density $\mathbf{B}(\mathbf{x})$ at each pixel position \mathbf{x} due to the electric current applied to the object boundary. Note only pixels on the object boundary will contribute to the magnetic field. Let S denote the set containing all the boundary pixels and s denote a boundary pixel. So, given current $I_{f(s)}$, the

magnetic flux density is computed as:

$$\mathbf{B}(\mathbf{x}) = \frac{\mu_0}{4\pi} \sum_{s \in S} I_{f(s)} \Gamma(s) \times \frac{\hat{\mathbf{R}}_{xs}}{R_{xs}^2}, \quad (12)$$

where $\Gamma(s)$ is the electric current vector at s and proportional to the edge strength, that is, $\Gamma(s) = (f(s)\mathbf{O}(s), 0)$, $\hat{\mathbf{R}}_{xs}$ is the unit vector from \mathbf{x} to s , and R_{xs} is the distance between them. Then, given the current I_C applied to the active contour C , its force field due to the magnetic field is:

$$\mathbf{F}(\mathbf{c}) = I_C \Upsilon(\mathbf{c}) \times \mathbf{B}(\mathbf{c}), \quad (13)$$

where $\Upsilon(\mathbf{c})$ denotes the electric current vector on the active contour position \mathbf{c} and is the rotated unit vector from $\nabla\Phi$. Note $\mathbf{F}(\mathbf{c})$ is always perpendicular to $\Upsilon(\mathbf{c})$, i.e. the force is always imposed in the contour normal inward or outward direction. Thus, the propagating contour will not suffer from saddle and stationary point issues, e.g. it will deal successfully with the four-disc problem. As the snake is embedded in the level set function and no longer considered as an explicit function, we also need to extend the forces imposed on the snake itself across the image domain in order to deform the level set function. This can be achieved using a force extension method such as [35], however, in this study we can simply treat each level set in Φ as a snake and compute its forces using (13). Thus, $\mathbf{F}(\mathbf{c})$ is extended to $\mathbf{F}(\mathbf{x})$, that is, across the image, i.e. $\mathbf{F}(\mathbf{c}) = (\mathbf{F}(\mathbf{x}), 0)$ where $\mathbf{c} = (\mathbf{x}, 0)$.

Given the force field $\mathbf{F}(\mathbf{x})$ derived from the magnetic interactions between the object boundary and the active contour, the evolving active contour under this force field is:

$$C_t = (\mathbf{F}(\mathbf{x}) \cdot \hat{\mathbf{N}}) \hat{\mathbf{N}}. \quad (14)$$

As contour smoothing is usually desirable, the standard curvature flow is added to rewrite the full MAC contour evolution formulation as:

$$C_t = \alpha g(\mathbf{x}) \kappa \hat{\mathbf{N}} + (1 - \alpha) (\mathbf{F}(\mathbf{x}) \cdot \hat{\mathbf{N}}) \hat{\mathbf{N}}, \quad (15)$$

where $g(\mathbf{x})$ is the stopping function as before. Its level set representation then takes this form:

$$\Phi_t = \alpha g(\mathbf{x}) \nabla \cdot \left(\frac{\nabla\Phi}{|\nabla\Phi|} \right) |\nabla\Phi| - (1 - \alpha) \mathbf{F}(\mathbf{x}) \cdot \nabla\Phi. \quad (16)$$

From (1), (4), and (6), we can see that DVF, GGVF, and CVF's external force fields are static with direction and magnitude based on spatial position only, hence the contour in these cases can not propagate through stationary or saddle points. In the geodesic model (see (2)) direction is solely based on the active contour but magnitude is based on the boundary, thus it can only monotonically expand or shrink and can not recover broken boundaries or be initialized across boundaries. The GeoGGVF (see (5)) is dominated by the external GGVF force but is conditionally influenced by a constant force imposed on the contour, however as the direction of the constant force is mainly determined by the external vector flow, it still can not resolve the topological issues of the static

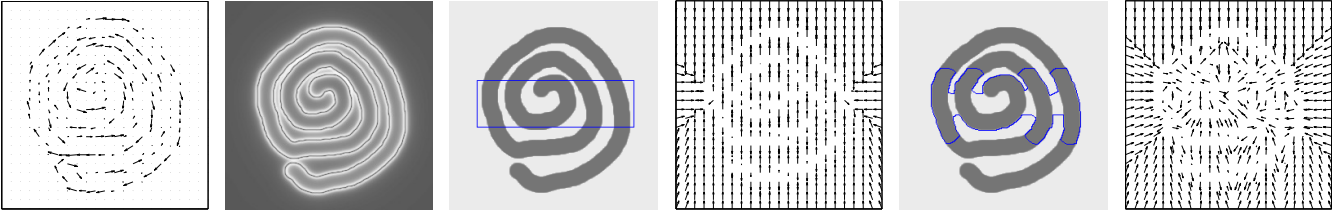


Fig. 3. From left: estimated boundary orientation, magnitude of the magnetic field, initial active contour, initial external force field, evolving contour, and its associated external force field. Final result is shown in the penultimate row of Fig. 4.

external force. In contrast to these models, MAC has the distinctive feature in that its direction relies on both spatial position and the evolving contour. The external bidirectional force is dynamically adaptive based on contour position (see 13), and equally importantly its direction is always normal to the evolving contour. The strength is determined by the magnitude of the magnetic field, thus the snake can be initialized across the object boundary and reach into concavities. Fig. 3 illustrates MAC's adaptive external force field.

3.3 Edge preserving magnetic force field diffusion

In keeping with other snake models based on image gradients, MAC can also suffer from image noise. Here, we perform anisotropic diffusion based on the idea in [2], [24] for the GVF/GGVF snakes to refine the magnetic force field when necessary. However, we modify the diffusion functions in order to better preserve edges and show that only diffusing a scalar field, rather than a vector field, is sufficient. Thus, there is also a gain in computational efficiency.

Note that the hypothesized magnetic forces are 3-dimensional in nature but perpendicular to the image plane, and we are only interested in the forces in the image plane. So, the magnetic flux density in (12) only has a non-zero component which is perpendicular to the image plane and we only need to diffuse the flux density along this direction. Thus, diffusing this component, denoted as $B(\mathbf{x})$, is equivalent to diffusing $\mathbf{B}(\mathbf{x})$ in the image plane. The diffused field $\hat{\mathcal{B}}(\mathbf{x})$, is the equilibrium solution of:

$$\mathcal{B}_t(\mathbf{x}) = p(B(\mathbf{x}))\Delta\mathcal{B}(\mathbf{x}) - q(B(\mathbf{x}))(\mathcal{B}(\mathbf{x}) - B(\mathbf{x})), \quad (17)$$

where $\mathcal{B}(\mathbf{x})$ is initially set to $B(\mathbf{x})$, and $p(B(\mathbf{x}))$ and $q(B(\mathbf{x}))$ are given as:

$$p(B(\mathbf{x})) = e^{-\frac{|B(\mathbf{x})|f(\mathbf{x})}{K}}, \quad q(B(\mathbf{x})) = 1 - p(B(\mathbf{x})), \quad (18)$$

Weighting the flux density magnitude with $f(\mathbf{x})$ in the diffusion term, $p(B(\mathbf{x}))$, ensures there is as little diffusion as possible at the object boundaries, while homogeneous areas will generally have small flux density due to a lack of support from edges, resulting in substantial diffusion. Examples of these are given later in Section 4.

3.4 Implementation

Object boundary description may be obtained using any standard edge detector, such as the Sobel filter as used in this paper. Some erroneous edges can be removed by dropping those with magnitude less than a very small percentage, say 10%, of the maximum magnitude. This also reduces later computational costs.

The main computational costs lay in two stages: evolving the level set function and computing the magnetic flux density. The Narrow Band approach [7] is used in order to save on costs associated with updating the level set function. The summation involved in the magnetic flux density computation (see (12)) is generally computationally expensive. However, this can be significantly reduced by letting only edge pixels be involved in the summation. More savings can be made by approximating the flux density based on interactions in a fixed radial distance R_c , instead of across the whole image, i.e. by replacing $\mathbf{s} \in \Omega_{f(s)}$ with $\mathbf{s} \in \Omega_{R_c}$ in (12). R_c should be reasonably large to prevent null flux density. In this paper, we used $R_c = 100$ throughout the experiments and found it a good tradeoff between accuracy and speed.

Alternatively, a slightly less precise but an even faster approach can be used based on the relationship between the magnetic field and the magnetic vector potential. The magnetic flux density can be calculated based on its magnetic vector potential $\mathbf{A}(\mathbf{x})$ [34]:

$$\mathbf{B}(\mathbf{x}) = \nabla \times \mathbf{A}(\mathbf{x}), \quad \mathbf{A}(\mathbf{x}) = \frac{\mu_0}{4\pi} \sum_{\mathbf{s} \in f(\mathbf{s})} I_{f(\mathbf{s})} \frac{\Gamma(\mathbf{s})}{R_{\mathbf{x}\mathbf{s}}}. \quad (19)$$

The magnetic vector potential can be decomposed into two orthogonal terms corresponding to the image coordinates, (i, j) , i.e. $\mathbf{A}(\mathbf{x}) = (A_i(\mathbf{x}), A_j(\mathbf{x}))$,

$$A_i(\mathbf{x}) = \frac{\mu_0}{4\pi} \sum_{\mathbf{s} \in f(\mathbf{s})} I_{f(\mathbf{s})} \frac{\gamma_i(\mathbf{s})}{R_{\mathbf{x}\mathbf{s}}}, \quad A_j(\mathbf{x}) = \frac{\mu_0}{4\pi} \sum_{\mathbf{s} \in f(\mathbf{s})} I_{f(\mathbf{s})} \frac{\gamma_j(\mathbf{s})}{R_{\mathbf{x}\mathbf{s}}}, \quad (20)$$

where $\gamma_i(\mathbf{s})$ and $\gamma_j(\mathbf{x})$ are the two corresponding orthogonal components of $\Gamma(\mathbf{s})$. Both of them take the same form as the Coulomb force potential [36]. Thus, the P³M method [36] can be used to efficiently approximate the magnetic vector potential by computing short range interactions exactly and long range interactions approximately as used in [29], [30]. We also note that equations

in (20) can each be viewed as a convolution with an inverse distance kernel. This can then be very efficiently solved in the frequency domain using FFT.

4 EXPERIMENTAL RESULTS

To objectively examine MAC's initialization invariancy and convergence ability, we first present results on various shape geometries and topologies using synthetic images with well-defined object boundaries. These include the four-disc problem, acute concavities, multiple objects with complex geometry and topology, and imperfect boundaries. More results, animations, and demonstration software can be found online².

The CPM model does not in general have topological issues when object boundaries are clearly defined, since unlike contour models its particles are manipulated individually. However, on real images where imperfect object boundaries, such as weak edges, often occur, CPM struggles to recover object shapes even after careful post-reconstruction. Thus, in subsections 4.1, 4.2, and 4.3, CPM is not considered. In 4.4, all methods reviewed earlier in Section 2, including CPM, are compared against each other in recovering objects with weak edges and broken boundaries. Subsections 4.5 and 4.6 demonstrate MAC's ability in handling even more arbitrary initializations and noise interference. Then, in 4.7, comparative analysis is performed on real images and more results of the proposed MAC model are presented. In 4.8, MAC is compared against region based methods, and the experiments are concluded in 4.9 with a discussion on parameter sensitivity and computational complexity.

4.1 The four-disc problem

Even though this is such a simple image and the active contour models are all using level set representation, convergence issues still arise. The solution becomes particularly challenging under certain initialization conditions. The first two rows in Fig. 4 show comparative recovered shapes for the DVF, geodesic, GGVF, GeoGGVF, CVF, and MAC models in columns (b) to (g) respectively. When the initial contour was placed outside the four discs (first row), only the geodesic snake and MAC could accurately recover them. However, in a more arbitrary cross-boundary initialization case (second row), only MAC was successful. The saddle and stationary points (see Fig. 1) prevented the other contours from recovering the discs. The geodesic active contour in this case simply disappeared after reaching the image borders.

4.2 Recovering acute concavities

Next, we consider the recovery of an acute concavity as shown in the third and fourth rows in Fig. 4, again with different initialization conditions. For the DVF, GGVF, and GeoGGVF snakes, their stationary vector force fields

exhibit stationary and saddle points, e.g. the saddle point at the entrance of the concave shape which prevents the snake converging to the object boundaries. Again, given an arbitrary cross-boundary initialization, the geodesic snake suffers severe problems and the constriction on the left side of the concave shape causes difficulties for the CVF active contour. MAC was the only active contour model that could successfully recover the shape in both initializations.

4.3 Handling complex geometries and topologies

When dealing with complex geometries, such as the swirl shape and the text "PAMI" shown in the last two rows in Fig. 4, MAC was the only model that managed to fully recover the shapes. The latter example further illustrates MAC's ability in dealing with multiple objects with complex topology.

Table 1 presents comparative results for the four-disc problem and recovering concavity and complex geometries with different initializations. The accuracy was measured by calculating the percentages of foreground pixels that were actually segmented as foreground (FG) and background (BG). The overall accuracy gives the measure for correctly segmented pixels given the total number of pixels in the image. The proposed MAC model significantly outperforms other boundary based snakes with a very high overall accuracy of 99.0% while the rest were well below 80%.

4.4 Recovery of broken boundaries and weak edges

Fig. 5 shows an S-shaped object with numerous breaks in its boundary. The geodesic and CVF snakes explicitly require there be no gaps along the object boundary. Thus, they will not be able to recover this S shape, no matter how much care is taken with their initialization. The GGVF and GeoGGVF snakes may be able to recover the shape with very careful initialization (notice there are several critical points due to the concave shape and curved body). CPM will rely purely on post-processing reconstruction as the particles alone can not close the boundary gaps. However, MAC can successfully recover the shape with any initialization condition, for example a small square contour initialized at the tip of the S.

To further illustrate the importance of bidirectionality and dynamic force fields, Fig. 6 shows a circular object with a partially blurred boundary segment, commonly used for weak-edge analysis, e.g. in [22], [23]. The geodesic snake in row (a) leaks through the weak edge due to the noisy stopping function. The GGVF and GeoGGVF snakes can converge to the weak edge with careful initialization due to their bidirectional force fields, however a more arbitrary initialization as seen in row (b) causes those snakes to collapse resulting in failure. The CVF snake requires a binary edge map without any gaps along the object boundary, which makes its use impractical in cases such as this one. Row

2. <http://vision.cs.bris.ac.uk/AC/MAC/>

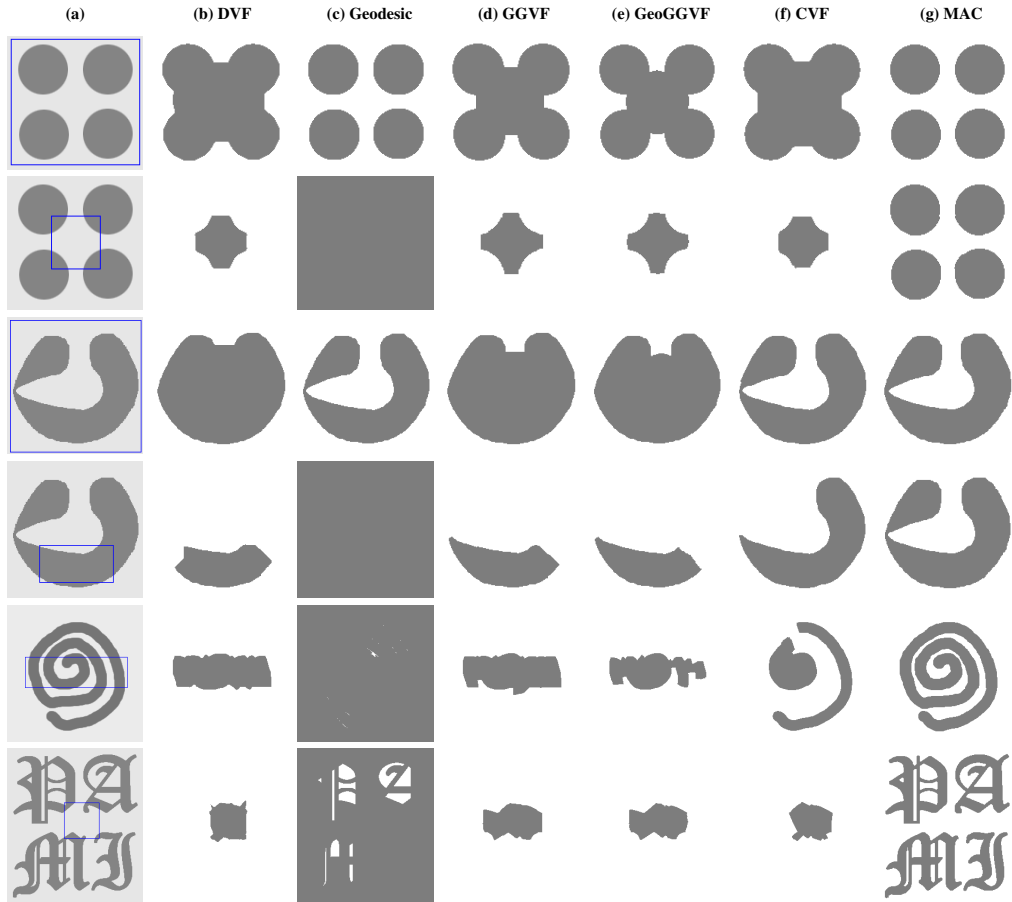


Fig. 4. Comparing shape recovery on synthetic images (by columns) - (a) initial snakes; (b) recovered shape using DVF, (c) geodesic, (d) GGVF, (e) GeoGGVF, (f) CVF, and (g) proposed MAC snakes.

TABLE 1
Comparative results on synthetic images (%).

	DVF	Geodesic	GGVF	GeoGGVF	CVF	MAC
Four-disc outside initialization	FG	100	100	99.2	100	99.3
	BG	69.9	97.9	74.0	79.5	70.9
	Overall	83.0	98.8	85.2	88.0	83.5
Four-disc cross initialization	FG	1.3	100	1.5	0.3	1.1
	BG	82.6	0	79.7	80.1	83.0
	Overall	47.3	43.4	45.8	45.5	47.5
Concavity outside initialization	FG	100	100	100	99.9	99.9
	BG	70.1	100	71.1	74.4	96.8
	Overall	82.4	100	83.0	84.8	98.0
Concavity cross initialization	FG	36.9	100	37.2	32.4	56.8
	BG	99.9	0	99.3	100	99.1
	Overall	73.7	41.0	75.3	74.9	90.2
Swirl cross initialization	FG	37.4	99.7	37.2	32.4	56.8
	BG	93.1	0	92.6	96.0	96.6
	Overall	76.2	30.3	75.8	76.7	84.5
PAMI cross initialization	FG	2.9	100	1.1	0.6	2.0
	BG	92.6	10.2	88.7	89.0	92.2
	Overall	61.8	41.0	58.7	58.6	61.2
Overall Average		70.7	59.1	70.6	71.4	77.5
						99.0

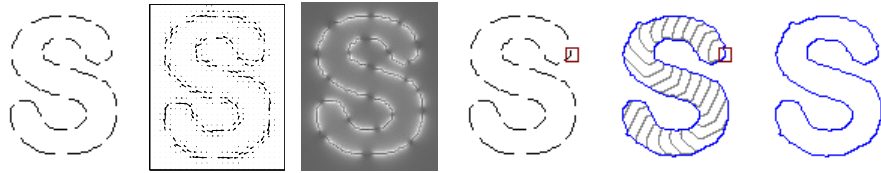


Fig. 5. Recovering an object with broken boundaries - from left: initial shape with 23 boundary gaps, estimated boundary orientation using chain codes, magnitude of the magnetic field, initial active contour, evolving contours, and stabilized MAC.

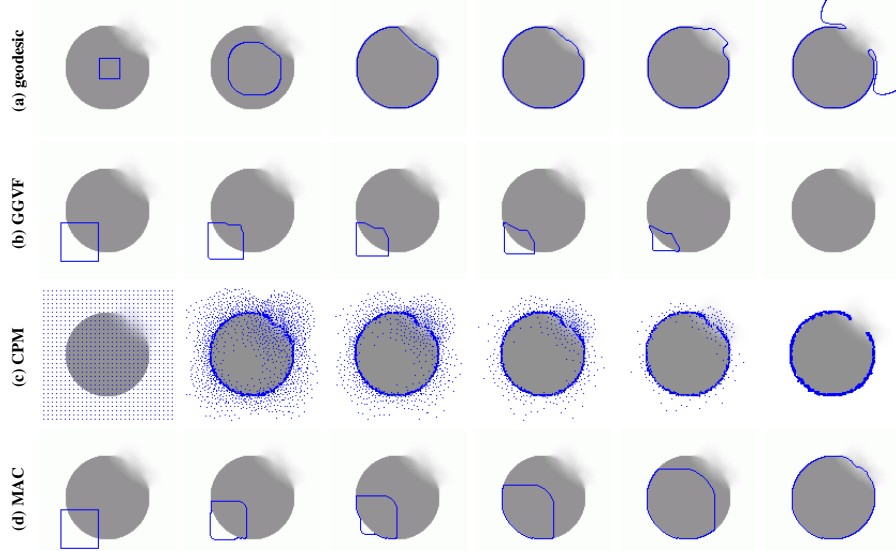


Fig. 6. Recovering an object with weak edges - (a) geodesic, (b) GGVF, (c) CPM, and (d) MAC snakes.

(c) shows CPM's particle evolution starting from a grid-like initialization across the whole image. In this case, the particles do not stop even after reaching the boundary as they are still under the influence of nearby boundaries. Thus, particles can not usually stabilize at weaker edges and move along towards stronger edges resulting in gaps. The gaps shown in row (c) can be closed with some post-processing, however in real images where weak edges often appear, the discontinuity can be so severe that it is beyond repair, as shown later in Subsection 4.7. MAC, on the other hand, does not suffer from these issues and can successfully localize the object, as shown in row (d).

4.5 Arbitrary initializations

In the previous examples, e.g. Fig. 4, we showed MAC's resilience to arbitrary initialization. Three more examples are given in Fig. 7. In the first row, the swirl shape is used with the initial snake just crossing the object. In the next row, several circular snakes were evenly distributed across the image domain. In the last row of Fig. 7, the same uniformly distributed initialization was used to recover the text "PAMI", which contains multiple objects and complex topology.

4.6 Noise sensitivity

The magnetic flux density diffusion described in Section 3.3 reduces MAC's sensitivity to noise. We corrupted the swirl shape image with Gaussian noise ranging from 10% ~ 50% of the pixels as shown in the first row of Fig. 8. The same initialization used in Fig. 4 was applied while also applying the same degree of flux density diffusion, i.e. $K = 0.2$ in (18). The results presented in the next row in Fig. 8 show little discernable differences. The overall accuracy only degraded slightly from 98.6% to 98.1%, while noise level increased significantly. Fig. 9 compares two horizontal profiles of before and after flux diffusion. The oscillation around zero magnetic flux magnitude in the original profile would introduce erroneous contours in the final snake segmentation. However, the proposed diffusion method removes undesirable noise but preserves true object boundaries. Although the proposed model can clearly handle a certain degree of noise interference, any snake reliant on image gradients will inevitably be affected by excessive noise corruption.

4.7 Experimental results on real images

Next, we show comparative results on real images containing weak edges and complex topologies with acute concavities. MAC was compared against all the methods

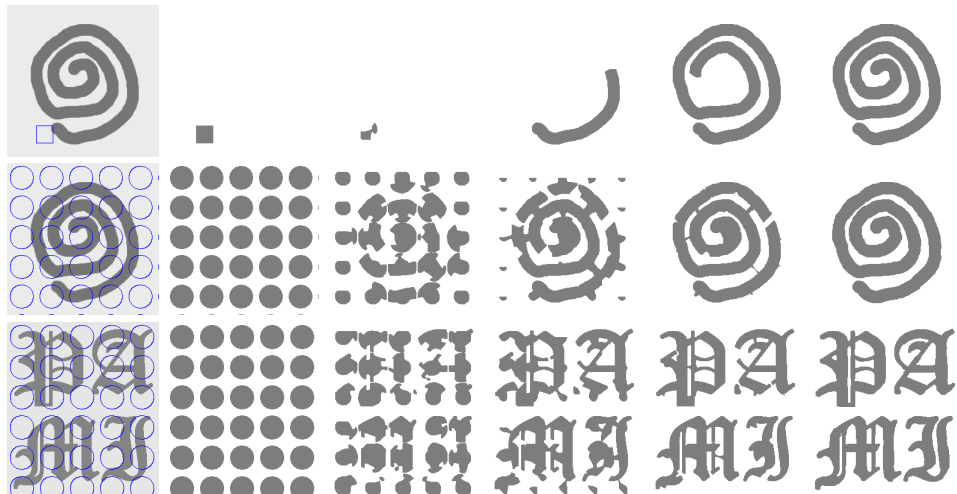


Fig. 7. Arbitrary initializations in MAC- first two rows: swirl shape using different initializations to Fig. 4; third row: complex shapes ("PAMI") using uniformly distributed circular snakes. The first column shows the initial snakes; second to fifth columns show intermediate stages; and the last column shows the recovered shapes.

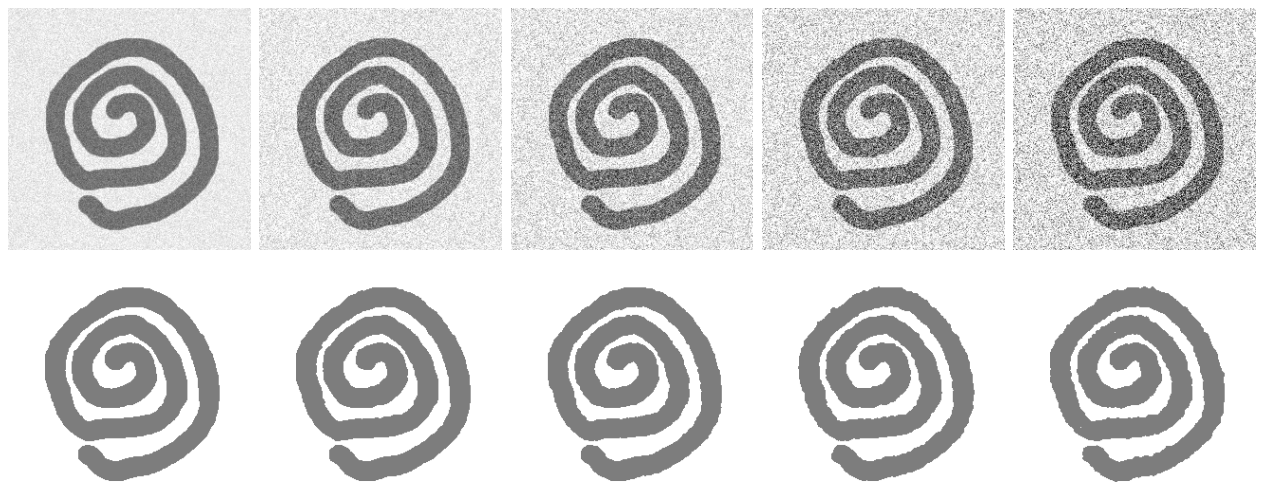


Fig. 8. Shape recovery with noise - first row: noise corrupted images ($10\% \rightarrow 50\%$ Gaussian noise in steps of 10); second row: recovered shapes. From left, overall accuracy compared to groundtruth: 98.6%, 98.4%, 98.4%, 98.2%, and 98.1%.

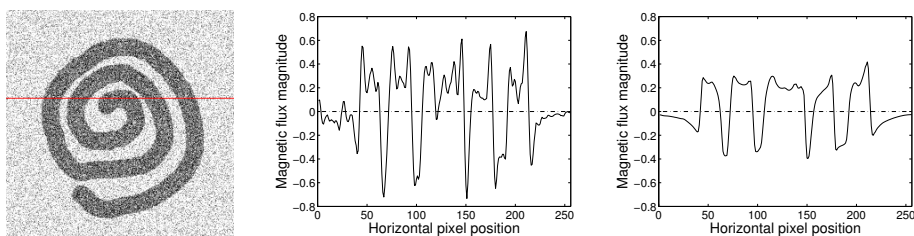


Fig. 9. Edge preserving magnetic flux diffusion - from left: A noise corrupted image with a highlighted scan line; Magnetic flux magnitude profile before diffusion; Magnetic flux magnitude profile after diffusion.

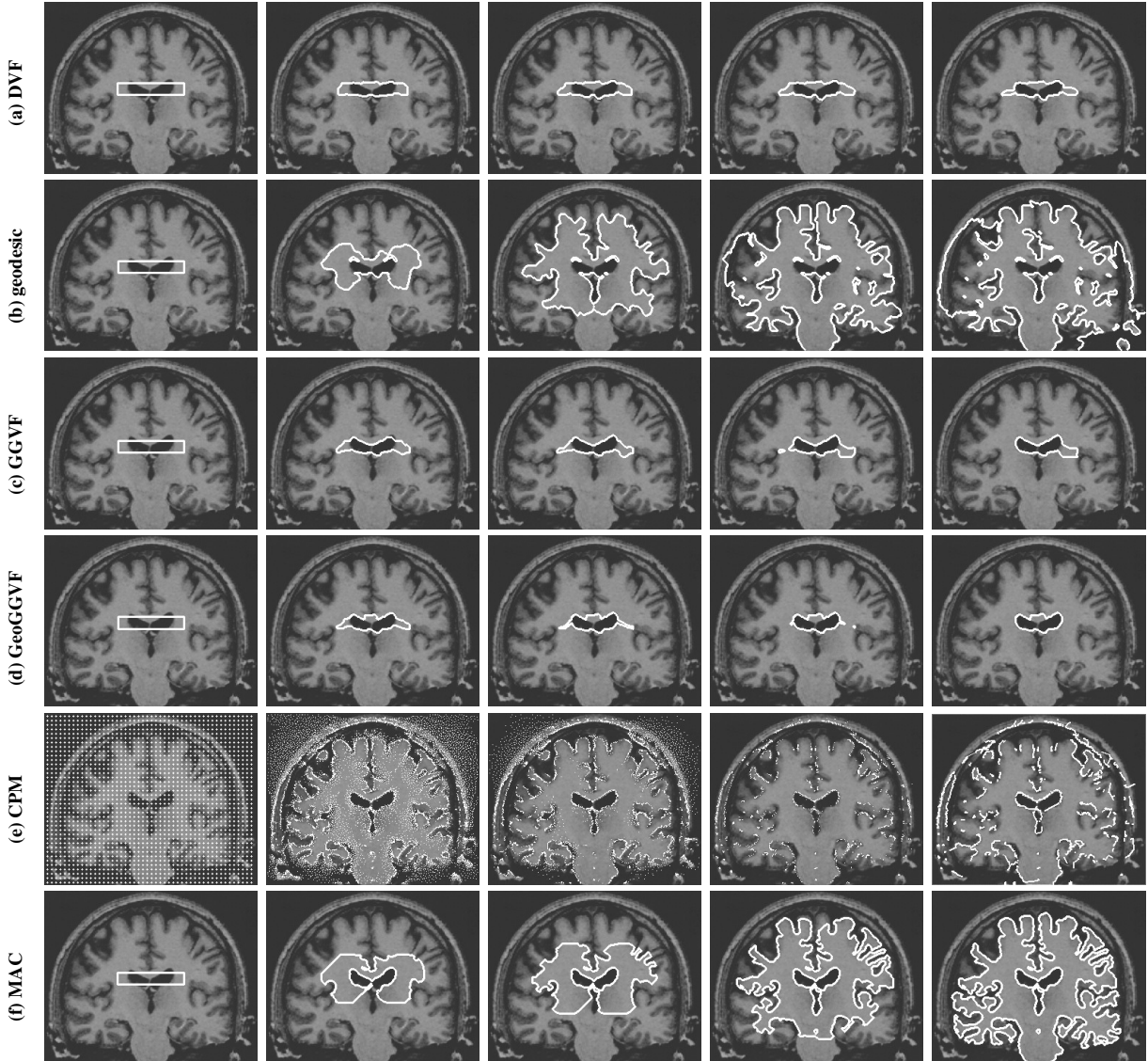


Fig. 10. Comparative study - results by row: (a) DVF, (b) geodesic, (c) GGVF, (d) GeoGGVF, (e) CPM, (f) MAC.

except the CVF snake, as CVF specifically requires closed binary object boundaries which we found difficult to obtain in our images. Fig. 10 shows a brain MRI image and its comparative segmentation results. For the active contour models, the snake was initialized across the left and right hemispheres, while for the particle model a grid of charges was used. The static vector force based methods (DVF, GGVF, and GeoGGVF) failed to evolve through the tortuous structures and collapsed to nearby edges as shown in rows (a), (c), and (d). The geodesic snake, in row (b), stepped across the weak edges but also failed to localize the boundaries. The free charges of CPM initially reached most of the object boundaries, but later failed to stabilize at weaker edges resulting in incomplete boundary description (row (e)). The MAC contours succeeded in evolving through the narrow and twisted structures as shown in row (f). Multiple regions were captured simultaneously.

In Fig. 11, another comparative example is given but

with the initial snake placed inside the object of interest without crossing the object boundaries. The DVF snake failed to evolve further once it was tangent to the underlying forces. GGVF and GeoGGVF suffered a similar problem and although finer parameter tuning might result in better results, the saddle and stationary points inside the object would inevitably lead to failure for both these snakes. CPM again struggled at weak edges neighboring strong edges and produced only partial recovery of the shape. Finally, MAC did not suffer from any of these problems and localized the object successfully.

More results using the proposed MAC model are shown in Fig. 12. None of the other methods we compared against could give satisfactory results in any of these cases, with some not even if they were very specifically initialized.

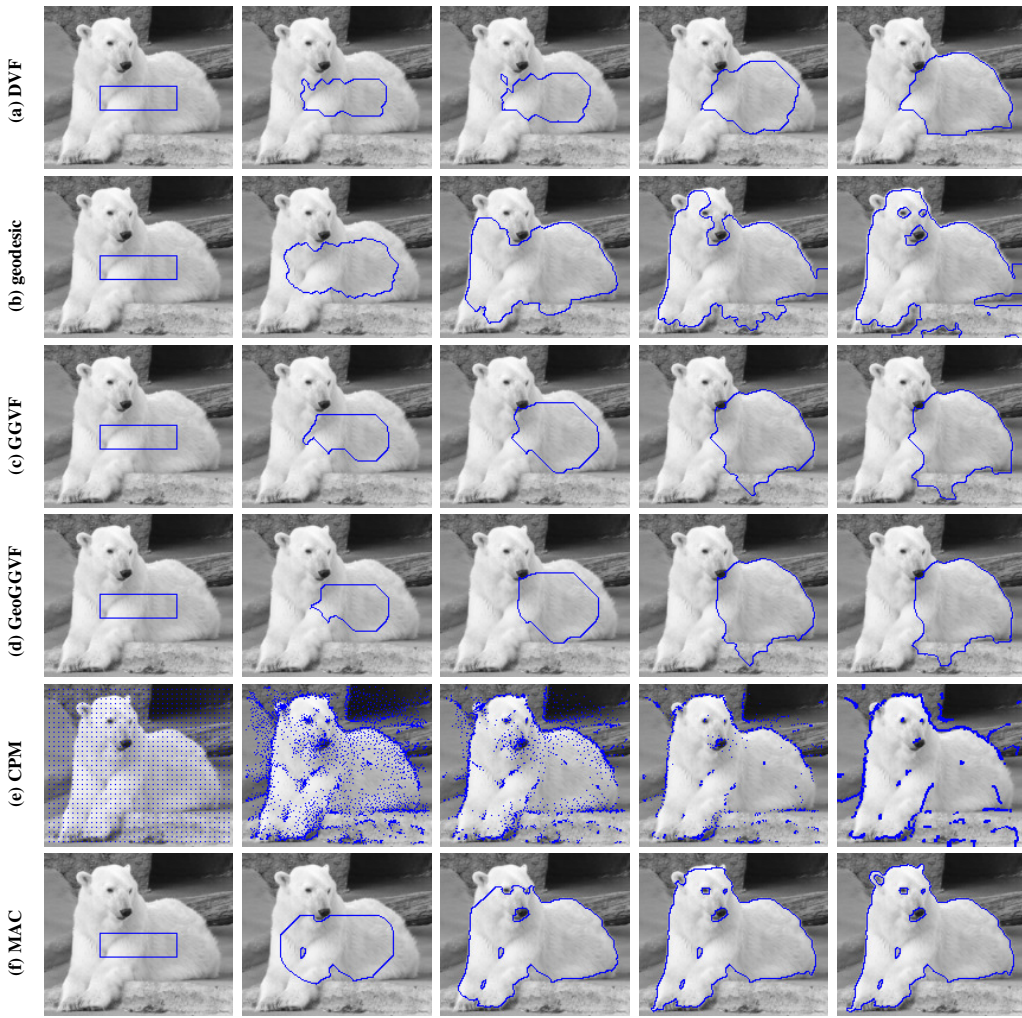


Fig. 11. Comparative study - results by row: (a) DVF, (b) geodesic, (c) GGVF snake, (d) GeoGGVF, (e) CPM, (f) MAC.

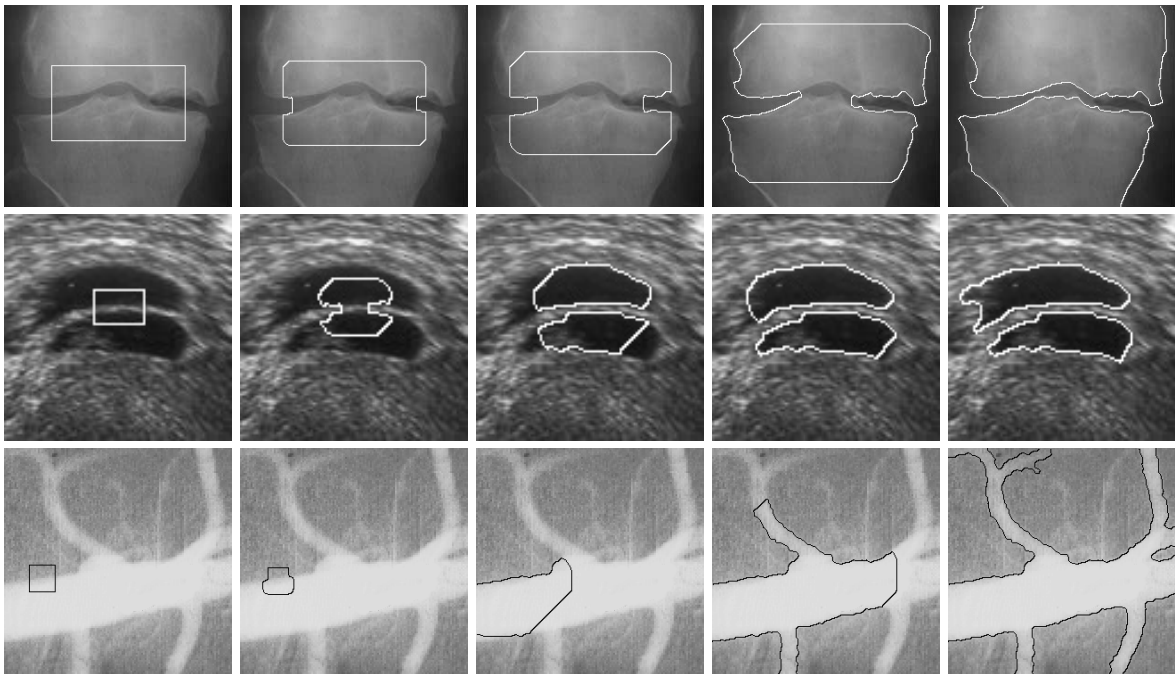


Fig. 12. More MAC examples on real images.

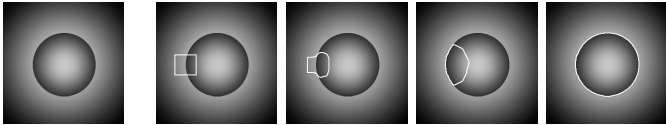


Fig. 13. Segmenting an object with non-uniform intensity and similar distribution to its background - From left: the original test image, initial MAC snake, evolving MAC snakes, and stabilized MAC snake.

4.8 Comparison to region based techniques

As discussed earlier in Section 1, region based techniques, such as [3], [15]–[19], generally use more global information in defining object boundaries. Common approaches include (i) global modeling of local statistics, such as intensity and filtering responses, followed by contour evolution based on object class probability [3], [17], (ii) evolving contours based on local region assumptions, e.g. piece-wise constant, and global energy optimization [15], [16], [19], and (iii) expanding contours subject to specific region uniformity criteria [18]. Also, there are some recent works imposing model knowledge while deforming contours e.g. [37]. This enhances the snake performance towards weak edges, noise interference, textured regions, and boundary occlusions. Due to their region indication function, these snakes can be initialized across object boundaries.

However, MAC as an image gradient based snake uses much simpler assumptions and less prior knowledge. It only assumes object boundaries collocating with intensity discontinuity. Region criteria, such as uniformity, is usually not universally applicable in object segmentation. Fig. 13 shows a simple object with non-uniform intensity but very similar intensity distribution to the background. The object boundary can be easily detected by examining the intensity discontinuity regardless of the similarities in regional statistics. Boundary based snakes also generally require less parameter tuning. For example, in the popular Mumford-Shah model, the scale parameter can significantly change the segmentation results. A lower value will allow more region boundaries to appear which can result in over-segmentation, and a higher value will produce a coarser segmentation with a risk of under-segmentation [38]. As demonstrated earlier, MAC can deal with broken boundaries and even disconnected object parts (see Fig. 5 for an example), which is difficult for region based techniques as object boundary description in such methods requires regional information support. One of the biggest advantages of region based techniques is their initialization and convergence ability. MAC has shown significant improvements over boundary based snakes and has very similar performance to region based techniques. Additionally, MAC is much easier to implement and more computationally efficient than most region based techniques.

Here, we provide a brief experimental comparison of the MAC model with a region based snake proposed

in [17]. The intensity distribution was modeled using Fuzzy C-means (here, we used Gaussian Mixture model (GMM) for better accuracy). The posterior probability was then used to propagate the contours (this is similar to [3] but not using texture information). The level set representation of the GMM region based snake is formulated as:

$$\Phi_t = \alpha \kappa |\nabla \Phi| + \frac{\beta}{1 - 2u(\mathbf{x})} |\nabla \Phi| - \nabla g(\mathbf{x}) \cdot \nabla \Phi, \quad (21)$$

where $u(\cdot)$ is the posterior probability of the region of interest. The first and third terms in (21) are designed for local regularization. The second term which is derived from the regional statistics is used to guide the contour to expand or shrink. Fig. 14 shows an example segmentation. Due to the nonuniformity, the GMM snake failed to correctly segment the object. Note that MAC was initialized across the boundary as well.

4.9 Parameter settings and computational complexity

The parameters for the MAC model are α , λ , and K . Parameter α appears in all level set based snakes and is used to control the contribution from curvature flow for smoothing. For most applications it can remain a constant. Parameter λ determines the edge orientation estimated as clockwise or anti-clockwise, one of which results in localizing objects and the other in localizing their background. This is application dependent and can be determined by the user. However, we can evolve two level sets simultaneously with the two possible λ values. Fig. 15 gives an example of using dual level sets. Different λ values produce two different magnetic flux density fields with the same magnitude but reversed directions across the image plane, according to (11) and (12), which results in opposite forces on the snake and hence two different contour evolutions (see Fig. 15). Parameter K is only used when noise interference is significant. In general, $K = 0.2$ is large enough to diffuse noise corruption as demonstrated in Fig. 8. In most cases, it may never be used.

MAC was developed in Java on a 2.8 GHz Pentium 4 running Linux. The main computational cost occurs at two stages: computing the magnetic field and evolving the level set embedded snake. The latter is similar to that of the geodesic snake, but MAC converges faster when near edges. For the former, a direct magnetic field computation is relatively expensive, e.g. 107s for the 254×193 pixel image shown in Fig. 15. This reduced to 44s when the magnetic interactions within a radial distance of 100 pixels only were computed. Alternatively, only 16s was required when using the P³M method or as little as 3s was needed for the FFT based method described in Subsection 3.4. More computational efficiency can be gained through code optimization and by implementing in a compiled language such as C.

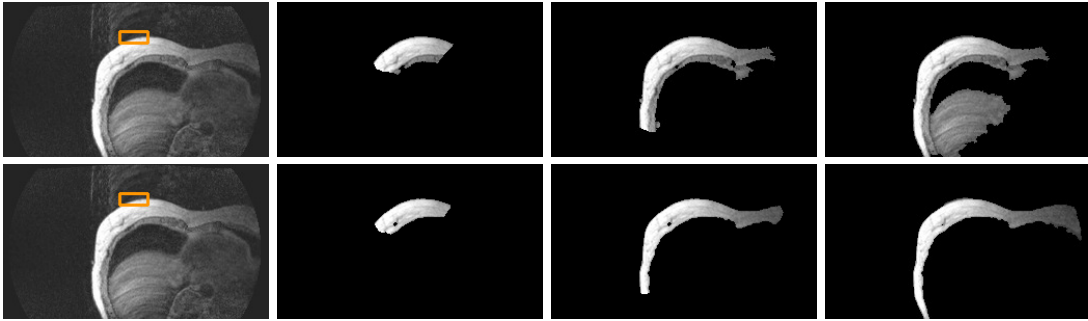


Fig. 14. Comparison with region based snake - Top row: initial GMM region based snake, segmented regions while evolving, and its stabilized segmentation; Bottom row: initial MAC snake, segmented regions while evolving, and stabilized MAC segmentation.

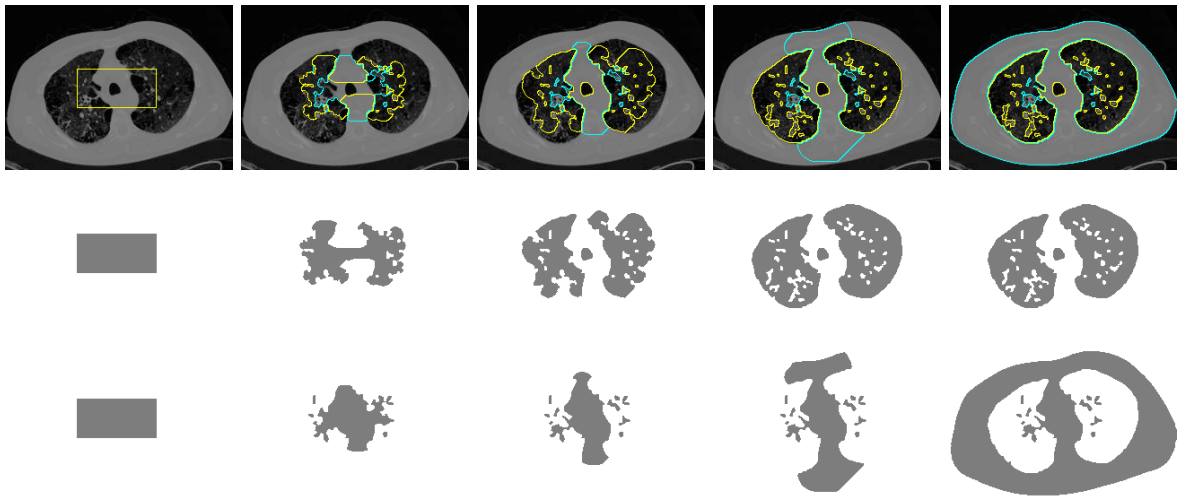


Fig. 15. MAC with dual level sets - first row: Initial MAC snake, evolution of dual MAC contours, and stabilized snakes in yellow and blue; second row: recovered shapes while evolving the first level set where $\lambda = 1$; third row: recovered shapes while evolving the second level set where $\lambda = 2$.

5 CONCLUSIONS

We proposed an active contour model using a novel external force field which is based on hypothesized magnetic interactions between the object boundary and the active contour. The MAC model can attract the contour into deep concave regions and does not suffer from saddle point and stationary point problems. Our comparative study showed significant improvement in initialization invariancy and convergence capability on existing state-of-the-art techniques.

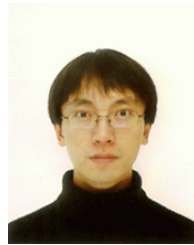
A fair computational performance comparison for all the snakes mentioned in this paper is rather difficult, if not naive, to contemplate. Not all the snakes are successful on the same image and except for MAC, all the other snakes require specific parameter tuning and/or careful initialization. However, a simple comparison was made on a 256×256 image containing a circular object which all the snakes could fully localize with the same initialization. The computational times on the same platform for the different snake models were: 28s for the DVF snake, 61s for the geodesic snake, 34s for the GGVF snake, 75s for the GeoGGVF snake, 95s for the

CVF snake (including around 60s spent on constructing its vector flow), and 38s for MAC.

The analogy of magnetic interaction between the active contour and the object boundaries works well. However, these interactions do not necessarily have to obey physical laws. In other words, we may modify the interactions in favor of our problem domain without maintaining their physical meaning. For example, R_{xs}^2 in (10) can be written in a general form as R_{xs}^n . The value of n will then affect the degradation rate of interaction forces in the image domain. By optimizing a cost function, we can find an optimum value for n . However, designing the cost function would involve defining "optimum" snake segmentation, which is a very difficult task and mostly application dependent. Also as part of our future work, we plan to extend the MAC model to deal with three dimensional data. The key extension lies in the estimation of boundary orientation in 3D.

REFERENCES

- [1] V. Caselles, R. Kimmel, and G. Sapiro, "Geodesic active contour," *IJCV*, vol. 22, no. 1, pp. 61–79, 1997.
- [2] C. Xu and J. Prince, "Generalized gradient vector flow external forces for active contours," *Signal Processing*, vol. 71, no. 2, pp. 131–139, 1998.
- [3] N. Paragios and R. Deriche, "Geodesic active regions and level set methods for supervised texture segmentation," *IJCV*, vol. 46, no. 3, pp. 223–247, 2002.
- [4] M. Kass, A. Witkin, and D. Terzopoulos, "Snakes: Active contour model," *IJCV*, vol. 1, no. 4, pp. 321–331, 1988.
- [5] P. Brigger, J. Hoeg, and M. Unser, "B-spline snakes: A flexible tool for parametric contour detection," *IEEE T-IP*, vol. 9, no. 9, pp. 1484–1496, 2000.
- [6] A. Clark and B. Thomas, "Evolving image segmentations for the analysis of video sequences," in *CVPR*, 2001, pp. 290–295.
- [7] J. Sethian, *Level Set Methods: Evolving Interfaces in Geometry, Fluid Mechanics, Computer Vision, and Materials Science*. CUP, 1996.
- [8] B. Morse, W. Liu, T. Yoo, and K. Subramanian, "Active contours using a constraint-based implicit representation," in *CVPR*, 2005, pp. 285–292.
- [9] L. Cohen and I. Cohen, "Finite-element methods for active contour models and balloons for 2-D and 3-D images," *IEEE T-PAMI*, vol. 15, no. 11, pp. 1131–1147, 1993.
- [10] O. Juan, R. Keriven, and G. Postelnicu, "Stochastic motion and the level set method in computer vision: Stochastic active contours," *IJCV*, vol. 69, no. 1, pp. 7–25, 2006.
- [11] K. Siddiqi, Y. Lauzière, A. Tannenbaum, and S. Zucker, "Area and length minimizing flows for shape segmentation," *IEEE T-IP*, vol. 7, no. 3, pp. 433–443, 1998.
- [12] N. Paragios, O. Mellina-Gottardo, and V. Ramesh, "Gradient vector flow geometric active contours," *IEEE T-PAMI*, vol. 26, no. 3, pp. 402–407, 2004.
- [13] C. Li, J. Liu, and M. Fox, "Segmentation of edge preserving gradient vector flow: an approach toward automatically initializing and splitting of snakes," in *CVPR*, 2005, pp. 162–167.
- [14] D. Tschumperlé, "Fast anisotropic smoothing of multi-valued images using curvature-preserving PDE's," *IJCV*, vol. 68, no. 1, pp. 65–82, 2006.
- [15] S. Zhu and A. Yuille, "Region competition: Unifying snakes, region growing, and Bayes/MDL for multiband image segmentation," *IEEE T-PAMI*, vol. 18, pp. 884–900, 1996.
- [16] T. Chan and L. Vese, "Active contours without edges," *IEEE T-IP*, vol. 10, no. 2, pp. 266–277, 2001.
- [17] J. Suri, "Two-dimensional fast magnetic resonance brain segmentation," *IEEE Engineering in Medicine and Biology*, vol. 20, no. 4, pp. 84–95, 2001.
- [18] X. Wang, L. He, and W. Wee, "Deformable contour model: A constrained optimization approach," *IJCV*, vol. 59, no. 1, pp. 87–108, 2004.
- [19] Z. Wang and B. Vemuri, "Tensor field segmentation using region based active contour model," in *ECCV*, 2004, pp. 304–315.
- [20] J. Haddon and J. Boyce, "Image segmentation by unifying region and boundary information," *IEEE T-PAMI*, vol. 12, pp. 929–948, 1990.
- [21] A. Chakraborty, H. Staib, and J. Duncan, "Deformable boundary finding in medical images by integrating gradient and region information," *IEEE T-MI*, vol. 15, no. 6, pp. 859–870, 1996.
- [22] X. Xie and M. Mirmehdi, "RAGS: Region-aided geometric snake," *IEEE T-IP*, vol. 13, no. 5, pp. 640–652, 2004.
- [23] C. Xu, J. Yezzi, and J. Prince, "On the relationship between parametric and geometric active contours," in *Proc. 34th Asilomar Conf. on Signal, Systems, and Computers*, 2000, pp. 483–489.
- [24] C. Xu and J. Prince, "Snakes, shapes, & gradient vector flow," *IEEE T-IP*, vol. 7, no. 3, pp. 359–369, 1998.
- [25] D. Gil and P. Radeva, "Curvature vector flow to assure convergent deformable models for shape modelling," in *EMMCVPR*, 2003, pp. 357–372.
- [26] B. Li and S. Acton, "Vector field convolution for image segmentation using snakes," in *ICIP*, 2006, pp. 1637–1640.
- [27] Y. Boykov and V. Kolmogorov, "Computing geodesics and minimal surfaces via graph cuts," in *ICCV*, 2003, pp. 26–33.
- [28] R. Ardon and L. Cohen, "Fast constrained surface extraction by minimal paths," *IJCV*, vol. 69, no. 1, pp. 127–136, 2006.
- [29] A. Jalba, M. Wilkinson, and J. Roerdink, "CPM: A deformable model for shape recovery and segmentation based on charged particles," *IEEE T-PAMI*, vol. 26, no. 10, pp. 1320–1335, 2004.
- [30] R. Yang, M. Mirmehdi, and X. Xie, "A charged active contour based on electrostatics," in *ACIVS*, 2006, pp. 173–184.
- [31] X. Xie and M. Mirmehdi, "Magnetostatic field for the active contour model: A study in convergence," in *BMVC*, 2006, pp. 127–136.
- [32] Y. Xiang, A. Chung, and J. Ye, "A new active contour method based on elastic interaction," in *CVPR*, 2005, pp. 452–457.
- [33] N. Ray and S. Acton, "Motion gradient vector flow: External force for tracking rolling leukocytes with shape & size constrained active contours," *IEEE T-MI*, vol. 23, no. 12, pp. 1466–1478, 2004.
- [34] D. Wolf, *Essentials of Electromagnetics for Engineering*. CUP, 2001.
- [35] D. Adalsteinsson and J. Sethian, "The fast construction of extension velocities in level set methods," *J. Comp. Phys.*, vol. 148, pp. 2–22, 1998.
- [36] L. Polloc and J. Glosli, "Comments on P3M, FMM, and the Ewald method for large periodic Coulombic systems," *Computer Physics Communications*, vol. 95, pp. 93–110, 1996.
- [37] D. Cremers, F. Tischhäuser, J. Weickert, and C. Schnörr, "Diffusion snakes: Introducing statistical shape knowledge into the Mumford-Shah functional," *IJCV*, vol. 50, no. 3, pp. 295–313, 2002.
- [38] G. Koepfler, C. Lopez, and J. Morel, "A multiscale algorithm for image segmentation by variational method," *Journal on Numerical Analysis*, vol. 31, no. 1, pp. 282–299, 1994.



Xianghua Xie received the M.Sc. (with commendation) and Ph.D. degrees in Computer Science in 2002 and 2006 respectively, from the University of Bristol, United Kingdom. He is currently an RCUK Academic Fellow in the Department of Computer Science, University of Wales Swansea, United Kingdom. He was previously a research associate in the Department of Computer Science, University of Bristol, United Kingdom. His current research interests are video analysis, texture analysis, image segmentation, surface inspection, deformable models, and historical document analysis. He is a member of the BMVA, IEE, and IEEE.



Majid Mirmehdi received the B.Sc. (Hons) and Ph.D. degrees in Computer Science in 1985 and 1991 respectively, from the City University, London. He has worked both in industry and in academia. He is currently a Reader in the Department of Computer Science at the University of Bristol, UK. His research interests include texture analysis, color image analysis, medical imaging, and document recognition. He has over 100 refereed conference and journal publications in these areas. He is an Associate Editor of the Pattern Analysis and Applications Journal. He is a member of the IEE, IEEE, and a member and the Chairman of the British Machine Vision Association.